Journal of Hazardous Materials 178 (2010) 644–651

Contents lists available at ScienceDirect

Journal of Hazardous Materials

journal homepage: www.elsevier.com/locate/jhazmat

# In situ DRIFT and kinetic studies of photocatalytic degradation on benzene vapor with visible-light-driven silver vanadates

Lung-Chuan Chen [a], Guan-Ting Pan [b], Thomas C.-K. Yang [b], Tsair-Wang Chung [c], Chao-Ming Huang [d,*]

[a] Department of Polymer Materials, Kun Shan University, Yung Kang City, Tainan, Taiwan
[b] Department of Chemical Engineering and Biotechnology, National Taipei University of Technology, Taipei, Taiwan
[c] Department of Chemical Engineering, Chung Yuan Christian University, Taoyuan, Taiwan
[d] Department of Environmental Engineering, Kun Shan University, Yung Kang City, Tainan, Taiwan

ARTICLE INFO

*Article history:*
Received 9 September 2009
Received in revised form 7 January 2010
Accepted 26 January 2010
Available online 2 February 2010

*Keywords:*
Photocatalyst
Visible-light irradiation
DRIFTS
Benzene

ABSTRACT

The visible-light active silver vanadates with different types of crystallines ($Ag_4V_2O_7$ and $Ag_3VO_4$ phases) were synthesized by an environmentally friendly aqueous process. The parameters of hydrothermal temperature and hydrothermal time were tuned to maximize the photocatalytic efficiency for the decomposition of benzene vapor under visible-light irradiation. The quantum efficiencies of the photocatalysts are compared on the basis of the crystalline phases, surface area, intensity of surface hydroxyl groups, and Brönsted acid sites. From the results of DRIFTS studies, the photocatalytic activities strongly depend on the intensities of the Brönsted acidity and hydroxyl groups presented on the silver vanadates. The sample synthesized at 140 °C and 4 h (HM140) exhibits the best photocatalytic activity; it has a reaction rate constant ($k_{app}$) of 1.42 $min^{-1}$, much higher than that of P25 ($k_{app}$ = 0.13 $min^{-1}$). For an irradiation time of 720 min, the mineralization yields of benzene were 48% and 11% for HM140 and P25, respectively. Based on the short-term decrease of benzene concentration and the long-term increase of $CO_2$ concentration, the photocatalytic ability of the HM140 sample is significantly superior to that of P25. The highest activity can be attributed to the synergetic effects of the richest Brönsted acid sites, and a favorable crystalline phase combined with abundant surface hydroxyl groups.



## 1. Introduction

Ag-containing monoclinic and perovskite materials, such as $AgTaO_3$ [1], $AgNbO_3$ [1], $AgInW_2O_8$ [2], and $Ag_3VO_4$ [3], have been proven to be good visible-light responsive photocatalysts in the field of the photocatalytic splitting of water into $H_2$ and $O_2$ but few studies have been conducted in the field of the photodecomposition of organic compounds [4–6]. For these silver oxide photocatalysts, the hybridization of the O $2p^6$ orbitals with Ag $4d^{10}$ results in the lifting up of the potential of the valence band, leading to a smaller band gap. Therefore, Ag-containing oxides are good for the use as visible-light responsive photocatalysts. However, the preparation procedures required the high purity powders and 850 °C (or higher) for 12 h, which restricted the development of solid-state reactions for industrial production. To reduce energy consumption, low-cost metal oxide catalysts with high visible-light photocatalytic activity are desirable. The hydrothermal method is considered a relatively simple and high yield process for growing various metal oxides at low temperature (less than 200 °C). The powders are prepared without high-temperature calcinations, leading to a reduction of energy consumption [7–10]. Moreover, a wide range of operating parameters, such as the concentrations of precursors, pH, synthesis temperature, and synthesis time, is easily controlled. The use of the hydrothermal method for the preparation of $Ag_3VO_4$ was firstly reported by Hu et al. [6]. They studied the effects of the ratio of silver to vanadium on the formation of $Ag_3VO_4$ and found that $Ag_3VO_4$ prepared in excessive vanadium at 160 °C for 48 h exhibited higher visible-light-driven activity than the sample prepared in a stoichiometric ratio. Huang et al. [11] investigated the effect of hydrothermal time on the hydrothermal-synthesis of silver vanadates and found that the powder synthesized at 140 °C for 4 h exhibited the highest photocatalytic activity.

Catalytic reactions generally occur on the surface of the catalyst; therefore, the photocatalytic activity strongly depends on the availability of active sites, which is related to the crystalline structure, specific surface area, and adsorption/desorption characteristics. Although surface area affects adsorption capacity, the chemical surface nature of a catalyst, such as the surface acidity/basicity, is considered crucial not only in determining adsorption capacity and reaction activity, but also in determining the reaction selectivity. However, previous research on silver vanadates has been

* Corresponding author at: No. 949 Da-Wan Rd. Yung-Kang City, Tainan 710, Taiwan. Tel.: +886 6 2050359; fax: +886 6 2050540.
*E-mail address:* charming@mail.ksu.edu.tw (C.-M. Huang).

0304-3894/$ – see front matter. 
doi:10.1016/j.jhazmat.2010.01.133

limited to correlating the nature of surface functional groups with photocatalytic kinetics.

In the present study, photodecomposition of benzene was selected as a model reaction to evaluate the photocatalytic performance of silver vanadates since benzene is widely used as a solvent in industrial processes. Benzene is also an in-door air pollutant which does not easily photo-decompose at relatively high concentrations. The reaction mechanism of the photodecomposition of benzene by the catalysts was discovered by a diffuse reflectance infrared Fourier transform spectroscopy and mass spectrometry (DRIFTS-MS) system. DRIFTS is one of the useful tools to simultaneously examine the interactions between adsorbates and the catalyst surface. Surface characterization combined with activity tests can provide insight into the effects of hydrothermal temperature and hydrothermal time on the phase formation and subsequently on the roles of surface hydroxyl groups and surface acidity in the reaction.

## 2. Experimental procedure

### 2.1. Synthesis

The hydrothermal synthesis of silver vanadates was performed using $AgNO_3$ and $NH_4VO_3$ as the silver and vanadium precursors, respectively. First, 0.006 mol $AgNO_3$ was dissolved into 60 mL of de-ionized water under stirring; 0.002 mol $NH_4VO_3$ was dissolved in hot de-ionized water (20 mL, 80 °C) to form a transparent solution, which was then cooled to room temperature. The aqueous $AgNO_3$ solution was added dropwise to the $NH_4VO_3$ solution under vigorous stirring for 0.5 h to make silver vanadium oxide suspension. The final pH value of the solution was adjusted to 7 using ammonia solution, followed by additional stirring at room temperature for 12 h. The as-obtained suspension was transferred into a Teflon liner autoclave, which was sealed and heated under various hydrothermal treatments (temperature: 120–180 °C, time: 2–8 h). After hydrothermal crystallization, the resulting precipitates were collected and washed repeatedly with de-ionized water three times, and then finally dried at 80 °C for 12 h.

### 2.2. Sample characterization

The X-ray diffraction (XRD) patterns of the powders were measured using an X-ray diffractometer (PANalytical X'Pert PRO) with Cu radiation ($\lambda = 0.15418$ nm) in the $2\theta$-range from 20° to 60°. In situ DRIFTS was used to investigate the surface hydroxyl groups and surface acidity of the catalysts. The measurements were performed using a PerkinElmer FTIR spectrometer (spectrum GX) and a praying mantis diffuse reflectance accessory (Harrick Scientific, DRP-PE9) with a controlled high-temperature and low-pressure reaction cell (Harrick Scientific, HVC-DRP-3). The DRIFTS cell (HVC-DRP-3) was equipped with an automatic temperature controller (ATC-024-1). Prior to the IR measurements, the samples were heated under vacuum from room temperature to 250 °C at 10 °C $min^{-1}$ in $N_2$ flow (30 mL $min^{-1}$), held at 250 °C for 30 min, and then cooled to 30 °C. DRIFT spectra were collected in the interval of 2800–4000 $cm^{-1}$ for surface hydroxyl groups and in the interval of 1000–2000 $cm^{-1}$ for surface acidity by averaging 64 scans with a resolution of 4 $cm^{-1}$.

The chemisorption of ammonia was employed as a measure of the surface acidity of catalysts. The catalyst was kept for 60 min under a flux of 5% (v/v) $NH_3/N_2$ (30 mL $min^{-1}$). At the end of the saturation process, the samples were flushed with $N_2$ flow (30 mL $min^{-1}$) for 10 min. Then, the samples were heated at a heating rate of 10 °C $min^{-1}$ and DRIFT spectra were collected until the samples were heated up to 250 °C; the samples were maintained at 250 °C for 30 min. The intensity of chemisorptions was determined based on the irreversible adsorption of ammonia. Infrared spectroscopic spectra of ammonia adsorbed on sample surfaces were subtracted from the reflectance spectra of the blank samples, which were collected as background reference spectra.

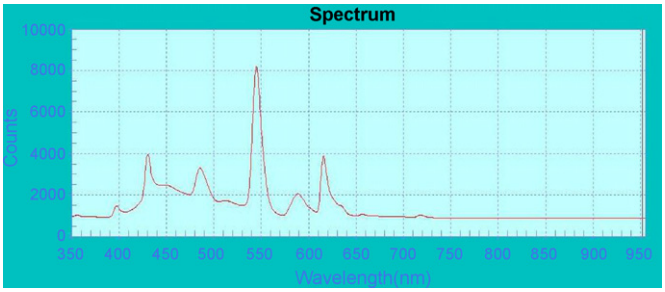


**Fig. 1.** The light spectra of the white fluorescent lamp used in this study. The major peaks were observed at 435, 485, 545, 587, and 615 nm.

UV–vis spectra were collected by a spectrophotometer (JASCO V-500) equipped with an integrated sphere assembly over the range of 400–700 nm. The specific surface areas of as-prepared powders were measured by nitrogen adsorption/desorption using the Barrett–Emmett–Teller (BET) method (Micromeritics ASAP 2020).

### 2.3. Photocatalytic activity evaluation with mass spectrometry

Photocatalytic activities of the samples were determined using the photodegradation of benzene under visible-light irradiation in a closed photoreactor. 0.05 g of photocatalyst powder was evenly dispersed in a thin film on an annular crystal tube [12]. Prior to the experiments, the sample was pre-treated at 150 °C for 30 min in dry $N_2$ (flowing at 100 mL $min^{-1}$), cooled to 30 °C, then exposed to $O_2$ flow (30 mL $min^{-1}$) for 60 min. Then, the inlet valve was closed and an appropriate amount of liquid benzene was injected into the reactor, producing the gaseous benzene concentration of 614 ppm. The photocatalytic reaction was carried out using a white daylight lamp (TFC, FL10W-EX) after the samples were kept in the dark for 60 min to achieve gas–solid adsorption equilibrium. The wavelength distribution of the white fluorescent lamp was shown in Fig. 1. The main emission band is occurred at 545 nm and the photon flux was measured as $3.98 \times 10^{-7}$ Einstein/s L. The compositions of the gaseous products were monitored on-line with a quadrupole mass spectrometer (SRS QMS300) at regular intervals.

## 3. Results and discussion

### 3.1. Effect of the hydrothermal temperature on structural, textural, and photocatalytic properties of silver vanadates

The XRD patterns of silver vanadates prepared at various hydrothermal temperatures for 4 h are shown in Fig. 2. Samples HM120, HM140, HM160, and HM180 correspond to hydrothermal temperatures of 120, 140, 160, and 180 °C, respectively. The diffraction peaks of silver vanadates prepared at various hydrothermal temperatures exhibit two sets of diffraction lines: one set of diffraction lines can be indexed well to the α-$Ag_3VO_4$ structure (JCPDS 43-0542), and the other weak diffraction lines are attributed to $Ag_4V_2O_7$ (JCPDS 77-0097). Therefore, the HM series samples had mixed phases of $Ag_4V_2O_7$ and α-$Ag_3VO_4$. The hydrothermal temperature did not have an obvious effect on the formation of silver vanadates. The corresponding crystallite sizes of HM120, HM140, HM160, and HM180 based on Scherrer's equation are listed in Table 1. The crystallite size of the samples increased with hydrothermal temperature, which implies that high hydrothermal

**Table 1**
Crystalline phases and crystal sizes of as-prepared silver vanadates.

| Sample | HM120 | HM140 | HM160 | HM180 | HT2 | HT6 | HT8 |
|---|---|---|---|---|---|---|---|
| Crystal phase | $Ag_3VO_4$ $Ag_4V_2O_7$ | $Ag_3VO_4$ $Ag_4V_2O_7$ | $Ag_3VO_4$ $Ag_4V_2O_7$ | $Ag_3VO_4$ $Ag_4V_2O_7$ | $Ag_3VO_4$ $Ag_4V_2O_7$ | $Ag_3VO_4$ | $Ag_3VO_4$ |
| Crystal size (nm) | 23.2 | 48.9 | 66.2 | 77.3 | 41.2 | 58.0 | 66.2 |

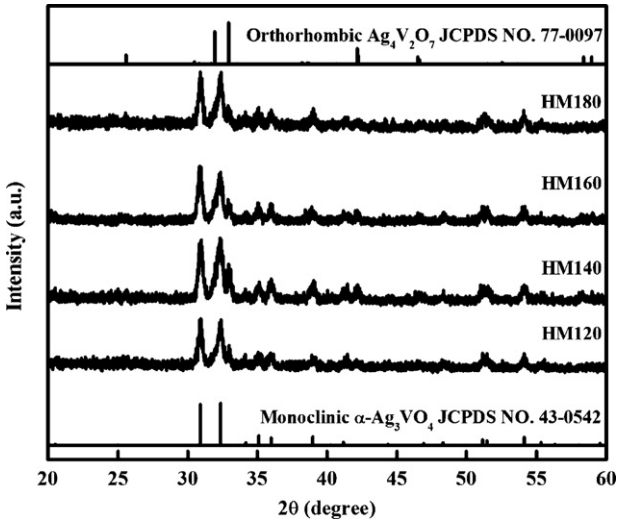


**Fig. 2.** XRD patterns of silver vanadates synthesized at various hydrothermal temperatures for 4 h.

temperature favored grain growth according to the theory of thermodynamic nucleation and growth.

Fig. 3 shows the results of benzene photodegradation for HM120, HM140, HM160, and HM180. Higher hydrothermal temperatures did not increase the benzene removal when the temperature was over 160 °C. Since the HM140 sample showed the highest photoactivity, the optimum temperature for hydrothermal-synthesis of silver vanadates was set at 140 °C. The specific surface areas of HM120, HM140, HM160, and HM180 are 6.9, 2.0, 1.3, and 1.0 $m^2 g^{-1}$, respectively, indicating that the specific surface area of HM140 is not associated with the photocatalytic activity.

### 3.2. Effect of the hydrothermal time on structural, textural, and photocatalytic properties of silver vanadate

To further investigate the formation process of silver vanadates, another series of samples was prepared at 140 °C for hydrothermal times of 2, 6, and 8 h; the samples were denoted as HT2, HT6, and HT8, respectively. The silver vanadates prepared at 140 °C for 4 h were the same as those for the HM140 sample. Fig. 4 shows the XRD patterns of silver vanadates obtained at various hydrothermal times at 140 °C. The HT2 samples had mixed phases of $Ag_4V_2O_7$ and α-$Ag_3VO_4$. However, at the hydrothermal time of 6 h, all the peaks attributed to $Ag_4V_2O_7$ disappeared and pure α-$Ag_3VO_4$ was obtained. At the hydrothermal time of 8 h, the HT8 sample had enhanced diffraction intensities of the α-$Ag_3VO_4$ crystal. The corresponding crystallite sizes of HT2, HM140, HT6, and HT8 are also listed in Table 1. The data show that the hydrothermal time had less influence on the crystal size than did the hydrothermal temperature. The specific surface areas of HT2, HM140, HT6, and HT8 are 3.2, 2.0, 1.7, and 1.4 $m^2 g^{-1}$, respectively. The photocatalytic activity of Degussa P25 was also studied for comparison with those of HT2, HM140, HT6, and HT8. The results are shown in Fig. 5. After 10 min of illumination, the HT2, HM140, HT6, and HT8 samples had much higher percentages of benzene removal than that of P25 (for example, 100% benzene removal for HM140 vs. 58% benzene removal for P25). The photocatalytic activity follows the sequence: HM140 > HT6 > HT8 > HT2 ≫ P25.

### 3.3. UV–vis diffusion reflectance spectra (UV–vis DRS)

The DRS spectra of as-prepared silver vanadates are shown in Fig. 6a and b. All hydrothermal synthesis samples had an intense absorption in the visible-light range. The onset positions of absorption edges for the samples prepared at various temperatures are similar, around 540 nm, which is equivalent to 2.3 eV, as shown in Fig. 6a. Significant differences in the absorption edges of the sam-

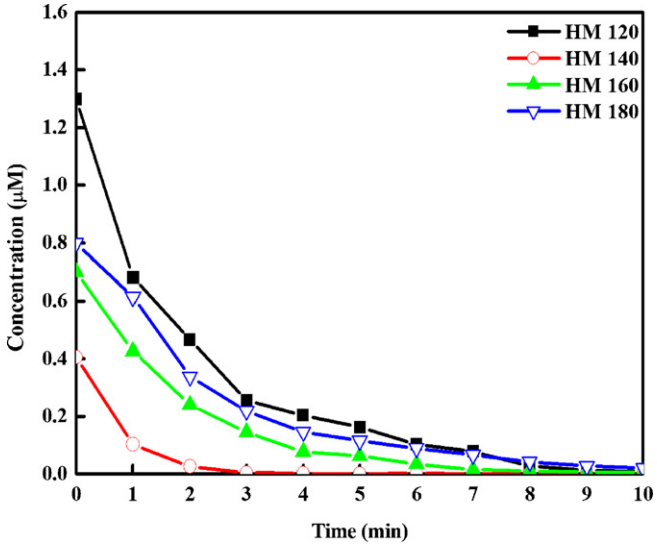


**Fig. 3.** Degradation curves of gaseous benzene decomposed by silver vanadates prepared at various temperatures.

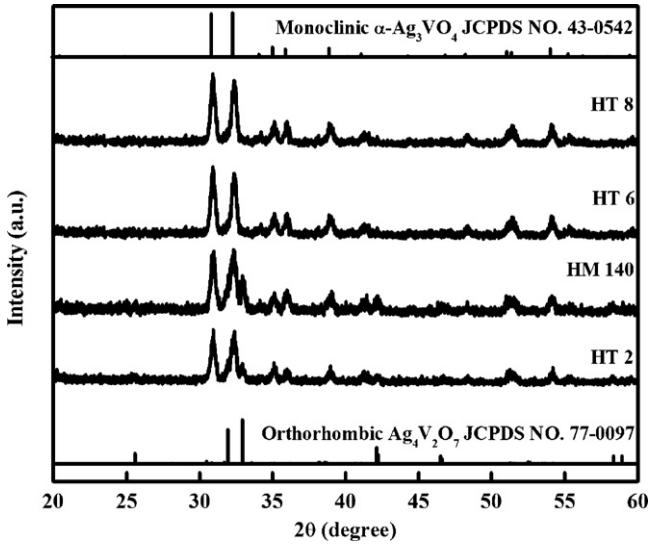


**Fig. 4.** XRD patterns of the silver vanadates synthesized at 140 °C for various hydrothermal times.

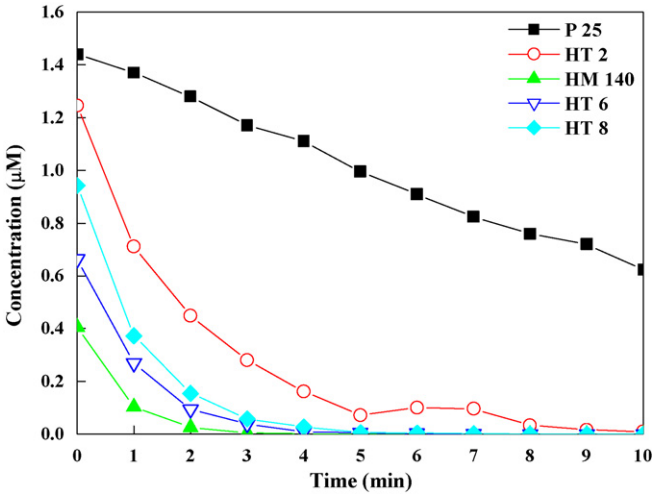


**Fig. 5.** Degradation curves of gaseous benzene decomposed by silver vanadates prepared at various hydrothermal times and by commercial $TiO_2$ (P25).

ples prepared at various hydrothermal times were observed. The differences in absorption edge wavelength for the silver vanadates, Fig. 6b, clearly indicate that four samples had different band gaps, which was due to the difference of crystalline structure. The spectra patterns of HT6 and HT8 were similar. Steep edges were observed

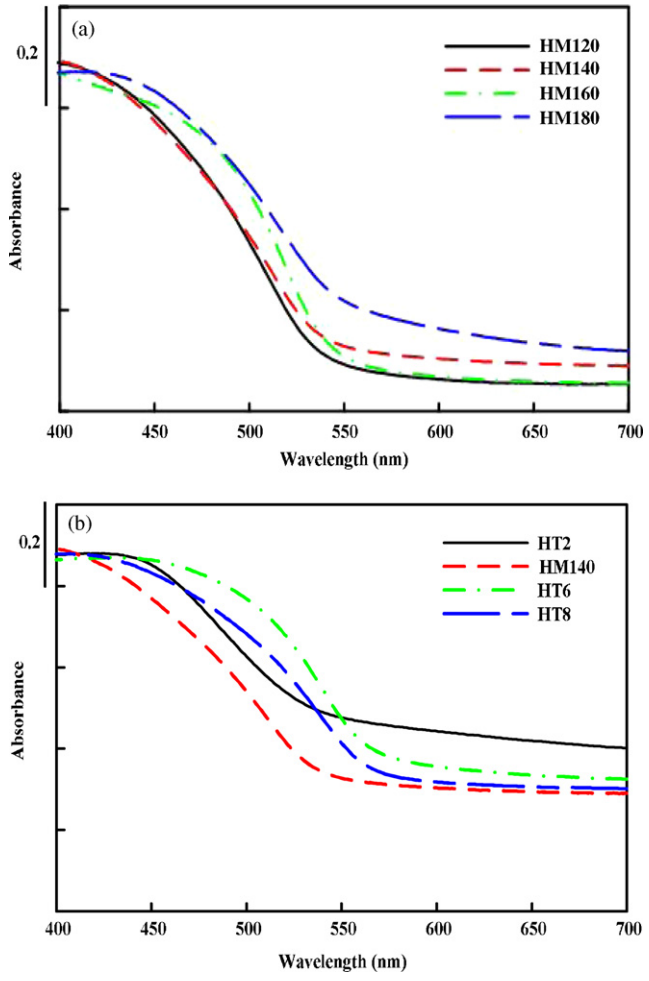


**Fig. 6.** UV–vis diffuse reflectance spectra of (a) HM series samples and (b) HT series samples.

**Table 2**
Apparent rate constants for the photodegradation of benzene.

| Sample | P25 | HM120 | HM140 | HM160 | HM180 | HT2 | HT6 | HT8 |
|---|---|---|---|---|---|---|---|---|
| $k_{app}$ ($min^{-1}$) | 0.13 | 0.46 | 1.42 | 0.51 | 0.41 | 0.54 | 0.99 | 0.94 |
| $R^2$ | 0.99 | 0.99 | 0.99 | 0.99 | 0.99 | 0.99 | 0.99 | 0.99 |

for samples synthesized for long times, reflecting the high crystallinity of the α-$Ag_3VO_4$ crystal. The band gap absorption edge of HT6 was determined to be 561 nm, equivalent to 2.2 eV of the band gap energy, which is in good agreement with that reported for $Ag_3VO_4$ [3].

### 3.4. Kinetic studies of the samples

The degradation data of benzene were fitted to a pseudo-first-order model. The degradation rate was obtained through linear fits of the expression: $\ln(C_0/C) = k_{app}t$ (where $C_0$ and $C$ are the concentration of benzene at reaction times 0 and $t$, respectively, and $k_{app}$ is the apparent rate constant). The apparent rate constants and the correlation coefficients ($R^2$) of the fitting are shown in Table 2. The $R^2$ values are all close to 1.0, implying that the pseudo-first-order kinetic model is suitable for the experimental data. Table 2 shows that the samples prepared at 120, 160, and 180 °C were not as active as the HM140 samples in terms of the degradation of benzene. Catalysts prepared with various hydrothermal times at 140 °C have higher photocatalytic activities than those of HM120, HM160, and HM180. For the closed reactor, HM140 had the maximum apparent rate constant, which was 11 times higher than that of P25.

Due to the complex mechanism of the photocatalytic reaction, the initial rate of photocatalytic reaction is usually used for the kinetic modeling of the photocatalytic process. Therefore, the Langmuir–Hinshelwood (L–H) model was chosen in this study; it is expressed as follows [13]:

$$r_0 = \frac{kKC_0}{1+KC_0} \quad \text{or} \quad \frac{1}{r_0} = \frac{1}{k} + \frac{1}{kK}\frac{1}{C_0} \tag{1}$$

where $r_0$ is the initial photocatalytic degradation rate of the reactant; $C_0$ is the initial reaction concentration of the reactant, $k$ is the reaction rate constant, and $K$ is the adsorption constant. $k$ and $K$ can be obtained by transforming the L–H equation into its inverse function as a linear relationship with an intercept of $k^{-1}$ and a slope $(kK)^{-1}$.

Since HM140 and HT2 had the maximum and minimum apparent rate constants, respectively, the analysis of the L–H model was applied to these samples. The kinetic parameters, such as reaction rate constant, adsorption constant, and correlation coefficient, are shown in Table 3. The correlation coefficients of HM2 and HM140 show that the photocatalytic degradation of benzene on silver vanadates matches the L–H model. According to the L–H model, the adsorption constant ($K$) reflects the adsorption affinity of adsorbate molecules with the adsorbent. It is generally accepted that a higher surface area of the catalyst leads to a higher reactant adsorption capacity. However, although P25 has the highest specific surface area (49.0 $m^2\,g^{-1}$), its adsorption constant was much lower than that of HM140, which had the highest adsorption capacity for benzene. The adsorption constant of HM140 was about 7 times higher than that of P25.

**Table 3**
Reaction rate constant ($k$) and adsorption equilibrium constant ($K$) of benzene for HT2, HM140, HT6, and P25.

| Sample | P25 | HT2 | HM140 | HT6 |
|---|---|---|---|---|
| $k$ (μM × $min^{-1}$) | 0.23 | 0.50 | 0.79 | 0.64 |
| $K$ ($\mu M^{-1}$) | 0.44 | 0.82 | 3.11 | 1.26 |
| $R^2$ | 0.95 | 0.99 | 0.99 | 0.98 |

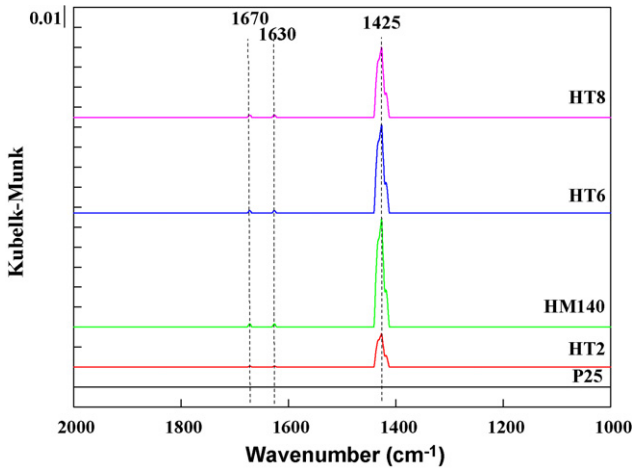


**Fig. 7.** DRIFT spectra of $NH_3$ species adsorbed on HT series samples and P25 samples heated at 250 °C.

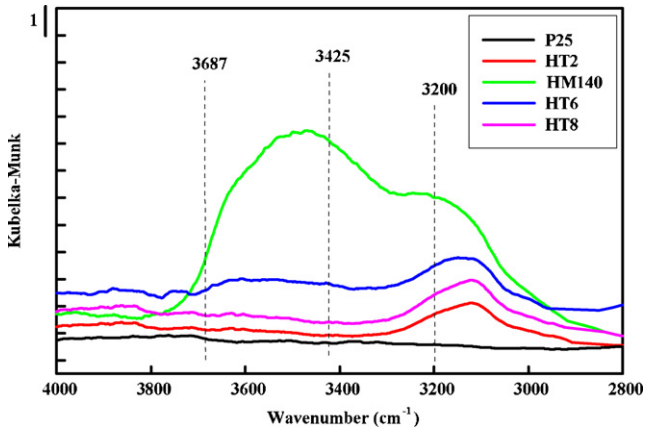


**Fig. 8.** Infrared spectra of OH groups on HT series samples and P25 samples heated at 250 °C.

### 3.5. Role of surface acidity

The equilibrium adsorption amount of volatile organic chemicals (VOC) in the dark provides a qualitative indication of the adsorption affinity between VOC and the photocatalyst. As shown in Fig. 5, the adsorption capacities of benzene on the samples, at the beginning of the photocatalytic reaction, decreased in the following sequence: HM140 > HT6 > HT8 > HT2 > P25. It is well known that either the adsorption process or the surface reaction is the rate-determining step for catalytic reactions; therefore, the photocatalytic reaction strongly depends on the crystalline structure, specific surface area, and adsorption/desorption characteristics. Yang et al. [14] reported that photocatalytic oxidation always begins with the adsorption process, which is the dye pre-adsorbed on $TiO_2$ for aqueous systems. However, in this study, the trends in the specific areas of the samples cannot explain the trends in benzene adsorption. Therefore, parameters other than surface area need to be investigated. The most important of them is the surface chemistry of the adsorbents used. A series of papers [15–18] has reported the Brönsted acidity of the catalysts is beneficial to the adsorption kinetics with adsorbates, which accelerates the reactions such as benzene hydrogenation, the oxidation of benzene, and alkylation of benzene.

To determine whether the surface chemistry of the catalysts affects the adsorption of benzene, ammonia adsorption on the photocatalysts surface was studied. A literature survey indicates that adsorption centers of $NH_3$ can be used to determine the presence of Brönsted and Lewis acid sites using DRIFT experiments [19–21]. Before the DRIFT measurements, the samples were saturated with $NH_3/N_2$, flushed with $N_2$ flow to remove the physical adsorption of ammonia, and then heated from 30 to 250 °C. The intensity of chemisorptions was determined based on the irreversible adsorption of ammonia. Fig. 7 shows the infrared spectra of ammonia adsorbed on HT series samples and P25 samples, which were heated at 250 °C for 30 min. The existence of $NH_4^+$ ions adsorbed onto Brönsted acid sites of the silver vanadate surfaces is supported by the presence of a band at 1425 $cm^{-1}$ due to the asymmetric deformation mode. A weak band at 1670 $cm^{-1}$ due to the symmetric deformation mode was also detectable [22,23]. The infrared spectra were obtained when the samples were heated at 250 °C for 30 min, indicating that the stability of the $NH_3$ adsorbed species was excellent and confirming the existence of Brönsted acidity of silver vanadates. On the other hand, no deformation modes regarding the $NH_4^+$ ions were observed for P25, indicating that P25 had few Brönsted acid sites. The intensity of Brönsted acid, detected at 1425 $cm^{-1}$, follows the sequence: HM140 > HT6 > HT8 ≫ HT2. Comparing Figs. 5 and 7, one can see that the adsorption capacity of benzene on silver vanadates closely correlates to the intensity of Brönsted acid of the samples. That is, a higher intensity of Brönsted acid of the silver vanadates indicates a larger adsorption capacity for benzene. As indicated in Table 3, the adsorption constant strongly depends on the surface acidity of silver vanadates.

### 3.6. Role of surface hydroxyl groups

In photocatalysis reactions, surface adsorbed water or the surface hydroxyl group acts as the trap for the photogenerated hole, forming oxidative hydroxyl radicals and subsequently oxidizing the adsorbed molecules on the substrate surface. Numerous studies have revealed that the nature and distribution of surface OH groups is the determining factor of the photocatalytic activity of $TiO_2$ [24–26]. Thus, FTIR studies were performed to characterize the distribution of hydroxyl groups present on HT series samples and to investigate whether hydroxyl groups were also responsible for the degradation ability of the silver vanadates. Before DRIFTS measurements, the samples were heated to 250 °C to remove adsorbed water. As shown in Fig. 8, two broad strong bands, ranging from 3700 to 3100 $cm^{-1}$, were observed for HM140, while a very weak band in the same range was observed for P25. The peaks in the range of 3700–3100 $cm^{-1}$ may be due to the overlapping of various OH groups. The deconvolution of the peak was conducted using several Gaussian curves based on the IR assignments of OH groups (at 3200, 3425, and 3687 $cm^{-1}$) reported in the literature.

The peak at 3200 $cm^{-1}$ is the typical OH group chemically adsorbed on the surface of the photocatalyst [27]. The peaks at 3425 and 3687 $cm^{-1}$ can be assigned to hydrogen bonded O–H stretching vibration [28] and linear $\nu$(OH) [29], respectively. The amounts of various OH groups on the HT series samples could be obtained by integrating the three individual curves, as shown in

**Table 4**
Various OH peaks in the IR spectrum, 2800–4000 $cm^{-1}$, calculated for HT series samples at 250 °C.

| Sample | Isolated-OH | | | Total area |
|---|---|---|---|---|
| | OH group chemically adsorbed at 3200 $cm^{-1}$ | H bonded O–H stretching vibration at 3425 $cm^{-1}$ | $\nu$(OH) linear at 3687 $cm^{-1}$ | |
| HT 2 | 101.08 | 22.74 | 2.30 | 126.12 |
| HM140 | 357.08 | 460.47 | 19.23 | 836.78 |
| HT 6 | 142.96 | 90.89 | 5.02 | 238.87 |
| HT 8 | 104.45 | 18.13 | 2.35 | 124.93 |

**Table 5**
Mineralization yield for various samples.

| Sample | Mineralization yield (%) |
|---|---|
| P25 | 11 |
| HM140 | 48 |
| HT6 | 19 |
| CTAB-SVO | 7 |

Table 4. A comparison of Tables 3 and 4 indicates that the amount of OH groups increases in the order of HT2 < HT6 < HM140, which agrees well with the rate constant results. Generally speaking, photocatalytic activity is related to the crystalline phase. Konta et al. [3] reported that α-$Ag_3VO_4$ showed stronger photocatalytic activity than those of β-$AgVO_3$ and $Ag_4V_2O_7$ for $O_2$ evolution from an aqueous silver nitrate solution under visible-light irradiation. For the HT series, it was observed that the HM140 sample, with mixed phases of $Ag_4V_2O_7$ and α-$Ag_3VO_4$, exhibits the highest photocatalytic activity, whereas HT6 shows low activity even though it has a high crystallinity of α-$Ag_3VO_4$. An increasing number of studies have indicated that a bicrystalline framework of anatase and rutile show much better photocatalytic activity than that of pure anatase $TiO_2$ [30–33]. Since nitrogen-doped $TiO_2$ has higher rutile content, it has more surface defects, which generate favorable active sites for trapping photogenerated holes. The holes are consequently transferred to hydroxyl groups to form hydroxyl radicals, resulting in higher photocatalytic efficiency. Apparently, the appropriate framework of $Ag_4V_2O_7$ and α-$Ag_3VO_4$ accompanied with abundant surface hydroxyl groups is vital for the photocatalytic efficiency of silver vanadates photocatalysts.

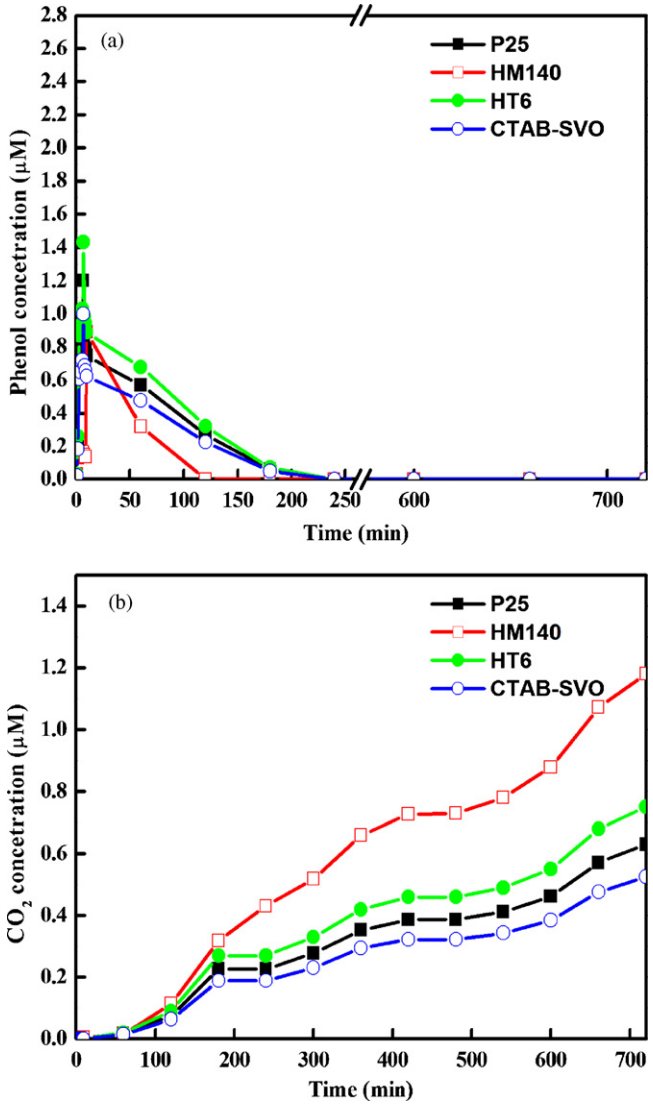


**Fig. 9.** Time-dependent concentrations for (a) phenol as main intermediate; (b) $CO_2$ as final product under visible-light irradiation.

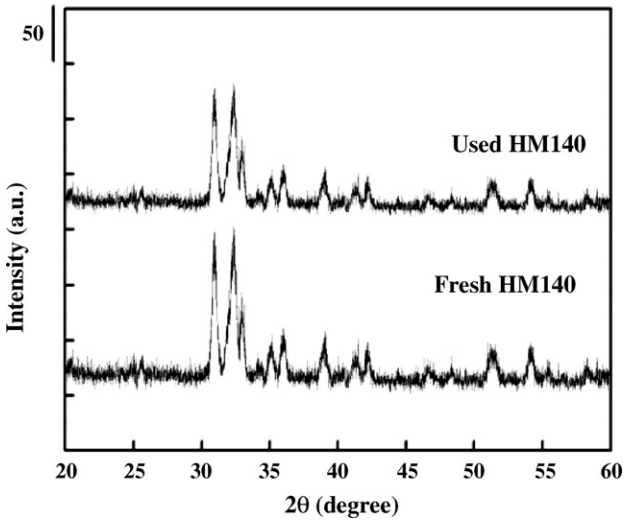


**Fig. 10.** XRD patterns of the fresh and used HM140 photocatalysts.

### 3.7. Intermediate, mineralization efficiency, and stability evaluation

As shown in Fig. 4, the XRD patterns of the samples synthesized at 140 °C for various durations consisted of pure α-$Ag_3VO_4$ or mixed phases of $Ag_4V_2O_7$ and α-$Ag_3VO_4$. The CTAB-SVO samples, prepared by the addition of cetyltrimethylammonium bromide (CTAB, $C_{19}H_{49}BrN$), were characterized to be the pure $Ag_4V_2O_7$ crystalline [34]. The GC/MS was used to investigate the intermediates or byproducts occurred during the photocatalytic oxidation of benzene. As observed in Fig. 9, phenol was detected to be the major by-product at the first 7 min of the photo-irradiation and it diminished to a very low concentration level after 60 min. Accordingly, the concentration of benzene dropped significantly at the same

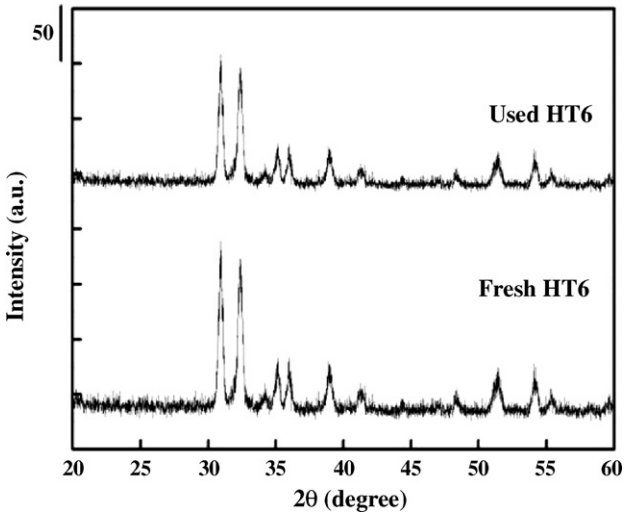


**Fig. 11.** XRD patterns of the fresh and used HT6 photocatalysts.

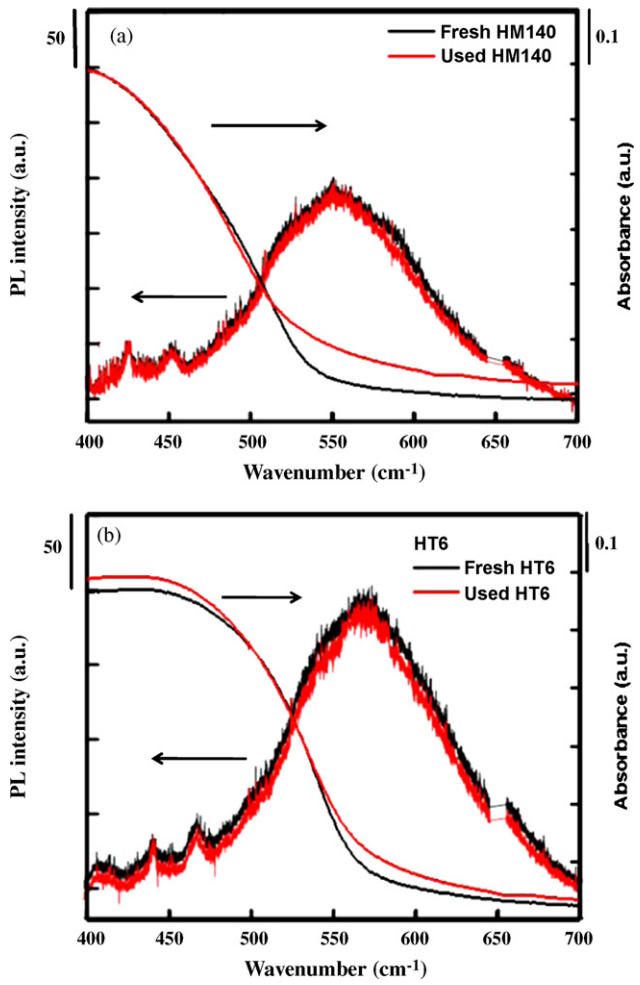


**Fig. 12.** Absorption and PL spectra for (a) fresh and used-HM140 catalysts; (b) fresh and used HT6 photocatalysts.

time when the formation of phenol was pronounced. Consistently, the carbon dioxide as the final product was found to be noticeable after 60 min of reaction. Similar results were also observed in the works of Wang and Ku [35]. Additionally, d'Hennezel et al. [36] reported that phenol was the major by-product, accompanied with very small amounts of hydroquinone and 1,4-benzoquinone as detected by GC/MS. Other researchers [37,38] reported that no gas-phase intermediates were detected by direct GC/FID analysis. For a 100% mineralization, six moles of carbon dioxide are formed from each mole of benzene. The results of mineralization yield under visible-light illumination are listed in Table 5. For an irradiation time of 720 min, the mineralization yields of benzene were 48% and 11% for HM140 and P25, respectively.

Since the benzene can be decomposed completely at the reaction run over 12 h, the reaction duration of 12 h is selected in the stability evaluation experiments. At the end of photocatalytic reaction, the photocatalyst was dehydrated at 120 °C for 6 h and then irradiated at UV light for 6 h. After the complete removal of the residuals on photocatalysts, the samples were reused again for photodegradation of benzene. After five times runs of reaction, the apparent rate constant and mineralization performance of the used HM140 under 720 min of irradiation were 1.41 $min^{-1}$ and 45%, respectively. Figs. 10–12 show the crystal structures, optical absorption, and photoluminescence spectra of the fresh and used HM140 and HT6. It can be seen that the crystal structure, optical absorption, photoluminescence spectra, and activity of the fresh and used silver vanadates are remained the same, indicating that these materials are quite stable.

## 4. Conclusions

Environmentally friendly silver vanadate photocatalysts were synthesized using hydrothermal synthesis without a high-temperature calcination process. Phenol as the by-product and the carbon dioxide as the final product were detected by GC/MS analysis during the oxidation of benzene. Based on the apparent rate constant for the initial photodegradation of benzene and $CO_2$ production after long-term light irradiation, the HM140 samples had high visible-light photocatalytic activity. HM140 has the richest Brönsted acid sites, which is advantageous for the adsorption of benzene, and because a favorable crystalline phase combined with abundant surface hydroxyl groups of HM140 increases the reaction rate. HT8 showed much lower activity even though it has the highest crystallinity of $\alpha$-$Ag_3VO_4$. In this study, the densities of Brönsted acid and OH groups had more influence on photocatalytic activity than did the crystalline structure. The results provide experimental evidence of the effects of crystal phases and surface chemistry on photocatalytic activity of visible-light active photocatalysts.

## Acknowledgement

We are grateful to the National Science Council, Taiwan, R.O.C., for providing research funding under grant NSC 96-2622-E-168-017-CC3.

## References

[1] H. Kato, H. Kobayashi, A. Kudo, Role of $Ag^+$ in the band structures and photocatalytic properties of $AgMO_3$ (M: Ta and Nb) with the perovskite structure, J. Phys. Chem. B 106 (2002) 12441–12447.
[2] J. Tang, Z. Zou, J. Ye, Photophysical and photocatalytic properties of $AgInW_2O_8$, J. Phys. Chem. B 107 (2003) 14265–14269.
[3] R. Konta, H. Kato, H. Kobayoshi, A. Kudo, Photophysical properties and photocatalytic activities under visible light irradiation of silver vanadates, Phys. Chem. Chem. Phys. 5 (2003) 3061–3065.
[4] X. Xu, C. Hu, Preparation and visible-light photocatalytic activity of $Ag_3VO_4$ powders, J. Solid State Chem. 180 (2007) 725–732.
[5] Y. Maruyama, H. Irie, K. Hashimoto, Visible light sensitive photocatalyst, delafossite structured $\alpha$-$AgGaO_2$, J. Phys. Chem. B 110 (2006) 23274–23278.
[6] X. Hu, C. Hu, J. Qu, Preparation and visible-light activity of silver vanadate for the degradation of pollutants, J. Hazard. Mater. 151 (2008) 17–25.
[7] J. Wang, S. Yin, T. Sato, Characterization and evaluation of fibrous $SrTiO_3$ prepared by hydrothermal process for the destruction of NO, J. Photochem. Photobiol. A: Chem. 187 (2007) 72–77.
[8] L. Ge, Novel Pd/$BiVO_4$ composite photocatalysts for efficient degradation of methyl orange under visible light irradiation, Mater. Chem. Phys. 107 (2008) 465–470.
[9] K.D. Witte, A.M. Busuioc, V. Meynen, M. Mertens, N. Bilba, G.V. Tendeloo, P. Cool, E.F. Vansant, Influence of the synthesis parameters of $TiO_2$-SBA-15 materials on the adsorption and photodegradation of rhodamine-6G, Microporous Mesoporous Mater. 110 (2008) 100–110.
[10] Y.C.M. Li, C.M. Huang, S.C. Wang, J.X. Wang, Hydrothermal synthesis and thermal decomposing method for synthesizing alumina nanorods, J. Inorg. Mater. 23 (1) (2008) 121–124.
[11] C.M. Huang, G.T. Pan, Y.C.M. Li, M.H. Li, T.C.K. Yang, Crystalline phases and photocatalytic activities of hydrothermal-synthesis $Ag_3VO_4$ and $Ag_4V_2O_7$ under visible light irradiation, Appl. Catal. A: Gen. 358 (2009) 164–172.
[12] G.T. Pan, C.M. Huang, L.C. Chen, W.T. Shiu, Immobilization of $TiO_2$ onto nonwoven fiber textile by silica sol: photocatalytic activity and durability studies, J. Environ. Eng. Manage. 16 (6) (2006) 413–420.
[13] M. Lewandowski, D.F. Ollis, A two-site kinetic model simulating apparent deactivation during photocatalytic oxidation of aromatics on titanium dioxide ($TiO_2$), Appl. Catal. B: Environ. 43 (2003) 309–327.
[14] T.C.K. Yang, S.F. Wang, S.H.Y. Tsai, S.Y. Lin, Intrinsic photocatalytic oxidation of the dye adsorbed on $TiO_2$ photocatalysts by diffuse reflectance infrared Fourier transform spectroscopy, Appl. Catal. B: Environ. 30 (2001) 293–301.
[15] O. Cairon, K. Thomas, A. Chambellan, T. Chevreau, Acid-catalysed benzene hydroconversion using various zeolites: Brönsted acidity, hydrogenation and side-reactions, Appl. Catal. A: Gen. 238 (2003) 167–183.
[16] V.I. Sobolev, K.A. Dubkov, E.A. Paukshtis, L.V. Pirutko, M.A. Rodkin, A.S. Kharitonov, G.I. Panov, On the role of Brönsted acidity in the oxidation of benzene to phenol by nitrous oxide, Appl. Catal. A: Gen. 141 (1996) 185–192.

[17] Y.C. Du, H. Wang, S. Chen, Study on alkylation of benzene with ethylene over β-zeolite catalyst to ethylbenzene by in situ IR, J. Mol. Catal. A: Chem. 179 (2002) 253–261.
[18] Y. Li, B. Xue, X. He, Synthesis of ethylbenzene by alkylation of benzene with diethyl carbonate over parent MCM-22 and hydrothermally treated MCM-22, J. Mol. Catal. A: Chem. 301 (2009) 106–113.
[19] M.R. Basila, T.R. Kantner, Infrared spectrum of ammonia adsorbed on silica-alumina, J. Phys. Chem. 71 (1967) 467–472.
[20] A. Satsuma, A. Hattori, K. Mizutani, A. Furuta, A. Miyamoto, T. Hattori, Y. Murakami, Surface active sites of vanadium pentoxide-tungsten trioxide catalysts, J. Phys. Chem. 92 (1988) 6052–6058.
[21] A. Zecchina, L. Marchese, S. Bordiga, C. Pazè, E. Gianotti, Vibrational spectroscopy of $NH_4^+$ ions in zeolitic materials: an IR study, J. Phys. Chem. B 101 (1997) 10128–10135.
[22] M.A. Centeno, I. Carrizosa, J.A. Odriozola, In situ DRIFTS study of the SCR reaction of NO with $NH_3$ in the presence of $O_2$ over lanthanide doped $V_2O_5/Al_2O_3$ catalysts, Appl. Catal. B: Environ. 19 (1998) 67–73.
[23] G. Ramis, L. Yi, G. Busca, Ammonia activation over catalysts for the selective catalytic reduction of $NO_x$ and the selective catalytic oxidation of $NH_3$. An FT-IR study, Catal. Today 28 (1996) 373–380.
[24] S.H. Szczcpankiewiecz, A.J. Colussi, M.R. Hoffmann, Infrared spectra of photoinduced species on hydroxylated titania surfaces, J. Phys. Chem. B 104 (2000) 9842–9850.
[25] G. Marcì, M. Addamo, V. Augugliaro, S. Coluccia, E. García-López, V. Loddo, G. Martra, L. Palmisano, M. Schiavello, Photocatalytic oxidation of toluene on irradiated $TiO_2$: comparison of degradation performance in humidified air, in water and in water containing a zwitterionic surfactant, J. Photochem. Photobiol. A 160 (2003) 105–114.
[26] J. Araña, C. Garriga i Cabo, J.M. Doña-Rodríguez, O. Gonzá lez-Díaz, J.A. Herrera-Melián, J. Pérez-Peña, FTIR study of formic acid interaction with $TiO_2$ and $TiO_2$ doped with Pd and Cu in photocatalytic processes, Appl. Surf. Sci. 239 (2004) 60–71.
[27] M. Janus, A.W. Morawski, New method of improving photocatalytic activity of commercial Degussa P25 for azo dyes decomposition, Appl. Catal. B: Environ. 75 (2007) 118–123.
[28] N.B. Colthup, L.H. Daly, S.E. Wiberley, Introduction to Infrared and Raman Spectroscopy, 3rd ed., Academic Press, Boston, 1990.
[29] J.M. Coronado, S. Kataoka, I. Tejedor-Tejedor, M.A. Anderson, Dynamic phenomena during the photocatalytic oxidation of ethanol and acetone over nanocrystalline $TiO_2$: simultaneous FTIR analysis of gas and surface species, J. Catal. 219 (2003) 219–230.
[30] Z. Ding, G.Q. Lu, P.F. Greenfield, Role of the crystallite phase of $TiO_2$ in heterogeneous photocatalysis for phenol oxidation in water, J. Phys. Chem. B 104 (2000) 4815–4820.
[31] D. Gumy, S.A. Giraldo, J. Rengifo, C. Pulgarin, Effect of suspended $TiO_2$ physicochemical characteristics on benzene derivatives photocatalytic degradation, Appl. Catal. B: Environ. 78 (2008) 19–29.
[32] G. Liu, Z. Chen, C. Dong, Y. Zhao, F. Li, G.Q. Lu, H.M. Cheng, Visible light photocatalyst: iodine-doped mesoporous titania with a bicrystalline framework, J. Phys. Chem. B 110 (2006) 20823–20828.
[33] G. Liu, X. Wang, Z. Chen, H.M. Cheng, G.Q. Lu, The role of crystal phase in determining photocatalytic activity of nitrogen doped $TiO_2$, J. Colloid Interface Sci. 329 (2009) 331–338.
[34] C.M. Huang, G.T. Pan, K.W. Cheng, W.S. Chang, T.C.K. Yang, CTAB-assisted hydrothermal synthesis of silver vanadates and their photocatalytic characterization, Chem. Eng. Sci. 65 (2010) 148–152.
[35] W. Wang, Y. Ku, Photocatalytic degradation of gaseous benzene in air streams by using an optical fiber photoreactor, J. Photochem. Photobiol. A: Chem. 159 (2003) 47–59.
[36] O. d'Hennezel, P. Pichat, D.F. Ollis, Benzene and toluene gas-phase photocatalytic degradation over $H_2O$ and HCL pretreated $TiO_2$: by-products and mechanisms, J. Photochem. Photobiol. A: Chem. 118 (1998) 197–204.
[37] X.Z. Fu, W. Zeltner, M.A. Anderson, The gas-phase photocatalytic mineralization of benzene on porous titania-based catalysts, Appl. Catal. B: Environ. 6 (1995) 209–224.
[38] J. Zhong, J. Wang, L. Tao, M. Gong, L. Zhimin, Y. Chen, Photocatalytic degradation of gaseous benzene over $TiO_2/Sr_2CeO_4$: kinetic model and degradation mechanisms, J. Hazard. Mater. B139 (2007) 323–331.